

# **Summer Internship Report**

## **Understanding the Broad-Line Region in Active galactic Nuclei and the techniques required in Reverberation Mapping**

By

Aditi Sinha,

Indian Institute of Science Education and Research, Kolkata



Under the supervision of

Dr. Suvendu Rakshit ,

Aryabhatta Research Institute of Observational Sciences, Nainital



May, 2022 - July, 2022

# ABSTRACT

Aim of this research project has been to study the properties of broad line region of Active Galactic Nuclei and to explore the techniques used in Reverberation Mapping. This study used the data from SDSS survey for 8 different quasars. The motivation behind has been to compare and see how well the techniques of ccf and Spectral analysis can be used in each of them. This report summarises the results obtained and also briefly compares it to a similar study done given in the publication - [2]. The code used can be found here - [GITHUB:Reverberation-Mapping](#)

# Contents

<b>1 CHAPTER 1 : INTRODUCTION</b>	<b>3</b>
1.1 Active Galactic Nuclei . . . . .	3
1.1.1 Seyfert Galaxies . . . . .	3
1.1.2 Quasars . . . . .	4
1.1.3 Radio Properties of Quasars . . . . .	5
1.2 Structure around a Blackhole . . . . .	7
1.3 Reverberation Mapping . . . . .	8
1.3.1 Assumptions . . . . .	8
1.3.2 Reverberation Results . . . . .	8
<b>2 Extracting Data and Modelling</b>	<b>10</b>
2.0.1 PCA Method . . . . .	10
2.0.2 Standardization . . . . .	11
2.0.3 Covariance Matrix . . . . .	11
2.0.4 Computing Eigenvectors and Eigenvalues . . . . .	11
<b>3 Data Analysis and Results</b>	<b>13</b>
3.0.1 RMID-101 Results . . . . .	14
3.0.2 RMID-191 Results . . . . .	15
3.0.3 RMID-229 Results . . . . .	16
3.0.4 RMID-267 Results . . . . .	17
3.0.5 RMID-272 Results . . . . .	18
3.0.6 RMID-694 Results . . . . .	19
3.0.7 RMID-772 Results . . . . .	20
3.0.8 RMID-840 Results . . . . .	21
<b>4 Lag Measurements</b>	<b>21</b>
4.1 Errors in Lag Measurements . . . . .	23
4.2 Lag Measurement for our data . . . . .	23
4.2.1 RMID - 101 . . . . .	24
4.2.2 RMID - 191 . . . . .	25
4.2.3 RMID-229 . . . . .	25
4.2.4 RMID-267 . . . . .	26
<b>5 Discussion</b>	<b>28</b>
<b>6 Acknowledgements</b>	<b>32</b>

# 1 CHAPTER 1 : INTRODUCTION

## 1.1 Active Galactic Nuclei

An Active Galactic Nuclei is a compact region at the center of galaxies which emits much more light than the rest of the galaxy combined, which can't be explained by the expected stars populating the region. AGNs are usually divided into two subclasses - **Seyfert Galaxies** and **quasars**. These two are divided on the basis of the amount of radiation emitted by the central source.

### 1.1.1 Seyfert Galaxies :

When the total energy emitted by the central region at visible wavelengths are comparable to the energy emitted by all the stars in the galaxy, such a galaxy is called the Seyfert Galaxies. A typical Optical Spectrum and an Ultraviolet Spectrum of such a galaxy is shown below :

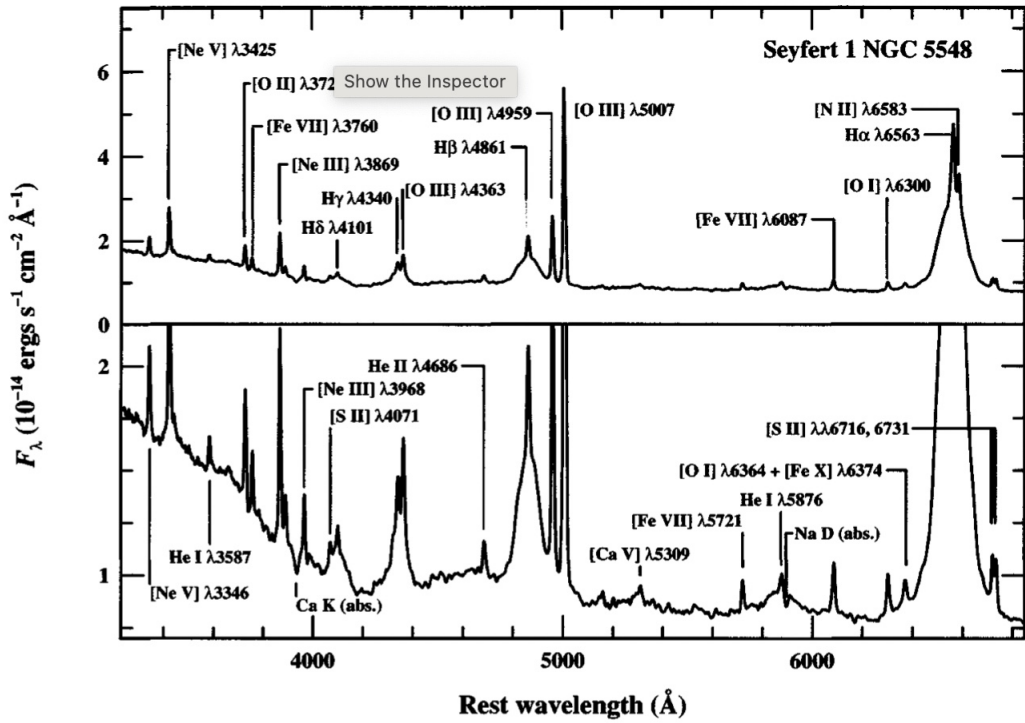


Figure 1: Optical Spectrum of Seyfert 1 Galaxy NGC 5548 where the prominent broad and narrow emission lines are strong absorption features of the host galaxy spectrum. Source : An Introduction to Active Galactic Nuclei, Bradley M. Peterson

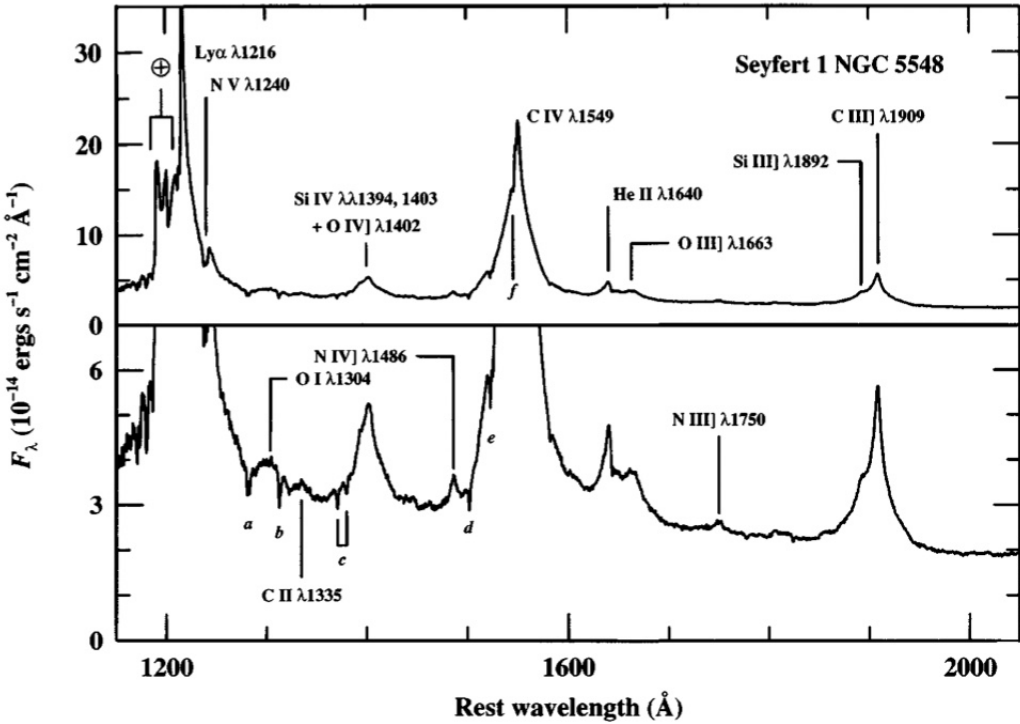


Figure 2: Ultraviolet Spectrum of Seyfert 1 Galaxy NGC 5548 where the prominent broad emission lines are labeled. Source : An Introduction to Active Galactic Nuclei, Bradley M. Peterson

### 1.1.2 Quasars

A Quasar is a galaxy in which the central nuclear source emits more radiation than all the stars in it by atleast a factor of 100. Hence, the quasars were not earlier related to Seyfert galaxies as they were not identified with galaxies before as they appeared as very big compact object with high luminosity. The light from the surrounding galaxy, because of its small angular size and relative faintness, is lost in the glare of the nucleus. Hence, the source looks 'quasi-stellar'.

The importance of Quasars include - extremely high luminosity implying physical extremes in the nearby Universe, and these can further help in serving as important cosmological probes, as they are identified at very large distances.

#### Properties of Quasars :

- Star-like objects identified with radio sources
- Time-variable continuum flux
- Large UV flux
- Broad emission lines
- Large redshifts

Unlike the stellar or galactic spectra, the AGN spectra cannot be described by blackbody emission at a single temperature which is suspected to be caused by non-thermall processes, primarily incoherent synchrotron radiation.

### 1.1.3 Radio Properties of Quasars :

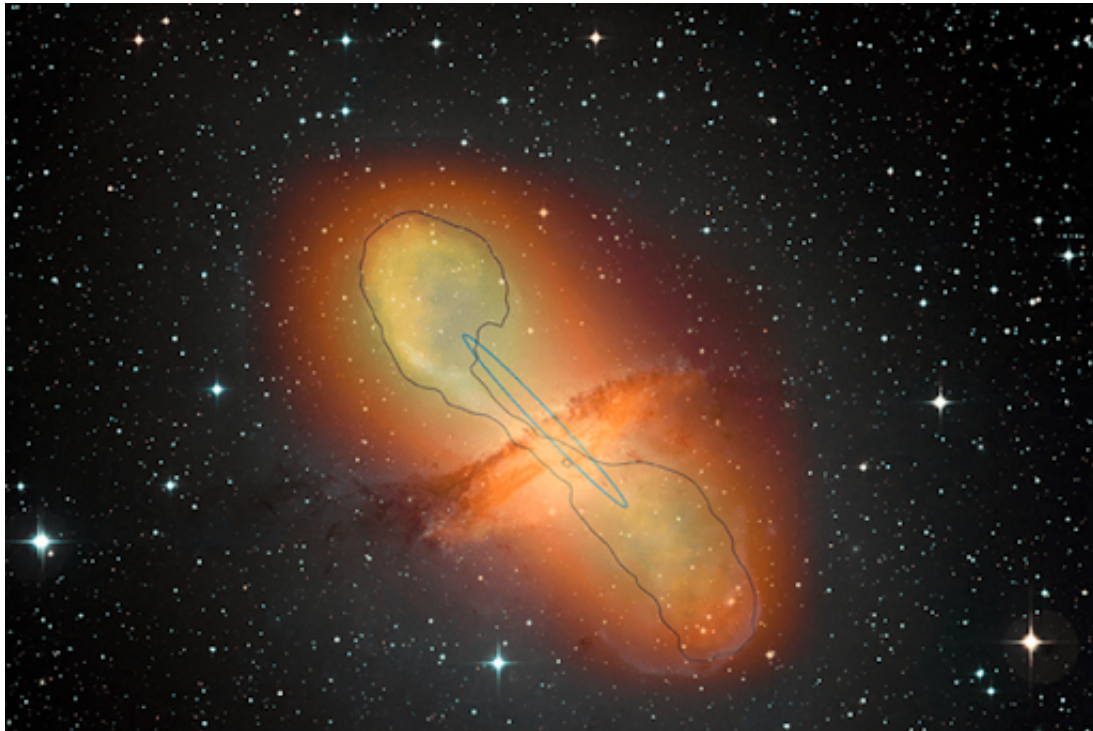


Figure 3: Radio Morphology of Quasars

The radio morphology of Quasars is often described by two components - “extended” and “compact” regions having different spectral properties. The extended component is described generally by two “lobes” of radio emission that are usually symmetrically located on either side of the nuclei. And the position of the optical quasar is generally coincident with that of the compact radio source. The major difference between the extended and compact components is that the extended component is optically thin to its own radio-energy synchrotron emission, whereas this is not true for the compact sources.

The Extended radio structures can be divided into two separate luminosity classes - Class I (FR I) sources are weaker radio sources which are brightest in the center, and has decreasing surface brightness towards the edges. Now, Class II(FR II) sources that are more luminous are limb-brightened, and often show regions of enhanced emission either at the edge of the radio structure or within the structure. Examples of both classes are shown below :

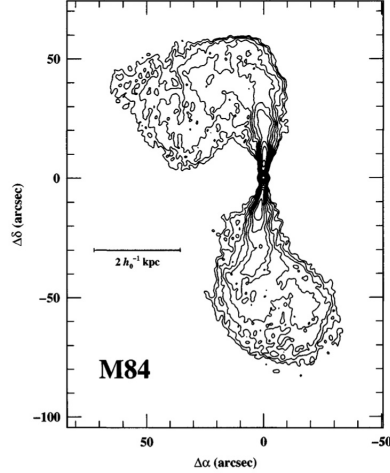


Figure 4: Example of an Fanaroff-Riley type I (FR I) galaxy

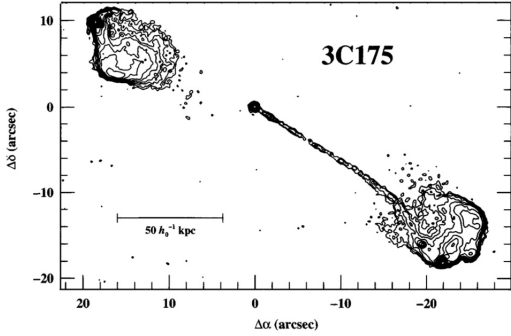


Figure 5: Example of Fanaroff-Riley type II (FR II) galaxy

Apart from the compact and extended components, we also have a feature called jets, that are simply extended linear structures. A jet is believed to originate at the central compact source and lead to the extended lobes. The appearance of jets suggests that they transport energy and particles from the compact source to the extended regions. Jets often appear on only one side of the radio source, and in cases where jets are seen on both sides one side (the 'counter-jet'), one side is much fainter than the other. The difference in brightness is thought to be primarily attributable to 'Doppler beaming' which preferentially enhances the surface brightness on the side that is approaching the observer.

The relative strength of the extended, compact, and jet components varies with frequency since the different components have different spectral shapes. The relative strengths also show considerable variation from source to source, with 'lobe-dominated' sources having steep spectra and 'core-dominated' sources having flat spectra. At least part of the observed differences among quasars must be due to orientation effects; whereas the extended components probably emit their radiation isotropically, the compact and jet components emit anisotropically.

The figure 5 shows a quasar coinciding itself with the bright compact source where a jet is observed on one side of the source. FR II sources are edge-brightened (probably due to

shock heating). Whereas the FR I sources are not edge-brightened and hence, the outflows are subsonic.

## 1.2 Structure around a Blackhole

Around the central region of a black hole, we have the accretion disk where the inflow of matter onto the central region occurs. Now, this region can be divided into mainly two parts, concerning our study - the Broad line Region (BLR) and the Narrow line Region(NLR).

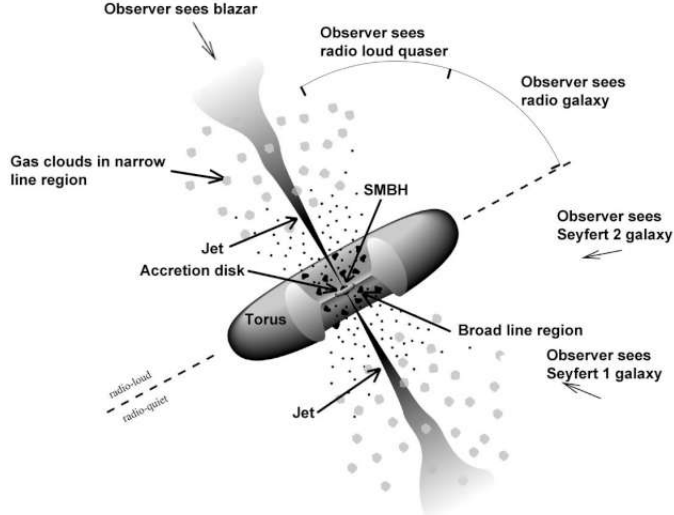


Figure 6: Structure surrounding a Blackhole - classification of the regions

Broad line Region is spatially unresolved in even the nearest AGNs. Hence, we do not have a detailed description of it.

However, looking at the light spectrum obtained from these Quasars, we see different emission lines and the related strengths. AGN emission-line spectra are kinematically composite. The narrow components have Doppler widths usually less than around  $500 \text{ km s}^{-1}$ ; these emission lines arise in relatively low-density ( $n_e \approx 10^3 \text{ cm}^{-3}$ ) gas that is spatially extended, as the narrow-line region (NLR) is at least partially resolved in some of the nearest AGNs. In contrast, the “broad components” have Doppler widths in the range 1000 to 25,000  $\text{km s}^{-1}$  and arise in gas of fairly high density (i.e.,  $n_e > 10^9 \text{ cm}^{-3}$ ).

Compared to the NLR, the actual amount of emission-line gas required to produce the broad emission lines can be quite modest as line emission is very efficient in high-density gases. There is also an important observation made - the line-emission fluxes have a short time delay as compared to the continuum flux. Now this delay can be attributed as the light travel time across the BLR i.e. -  $\tau = \frac{R}{c}$ .

### 1.3 Reverberation Mapping

Now, as we talked about in the previous section, there is a time delay and we use it to measuring the structure around Broad Line Region. Now, this procedure is termed as **Reverberation Mapping**. It is also the primary technique to estimate the Black hole masses. There are certain Assumptions that are used -

#### 1.3.1 Assumptions

- The continuum originates in a single central source.
- The light travel time across the BLR is the most important time scale.
- There is a simple, though not necessarily linear, relationship between the observed continuum and the ionizing continuum.

#### 1.3.2 Reverberation Results

- Size of the BLR and scaling it with Luminosity

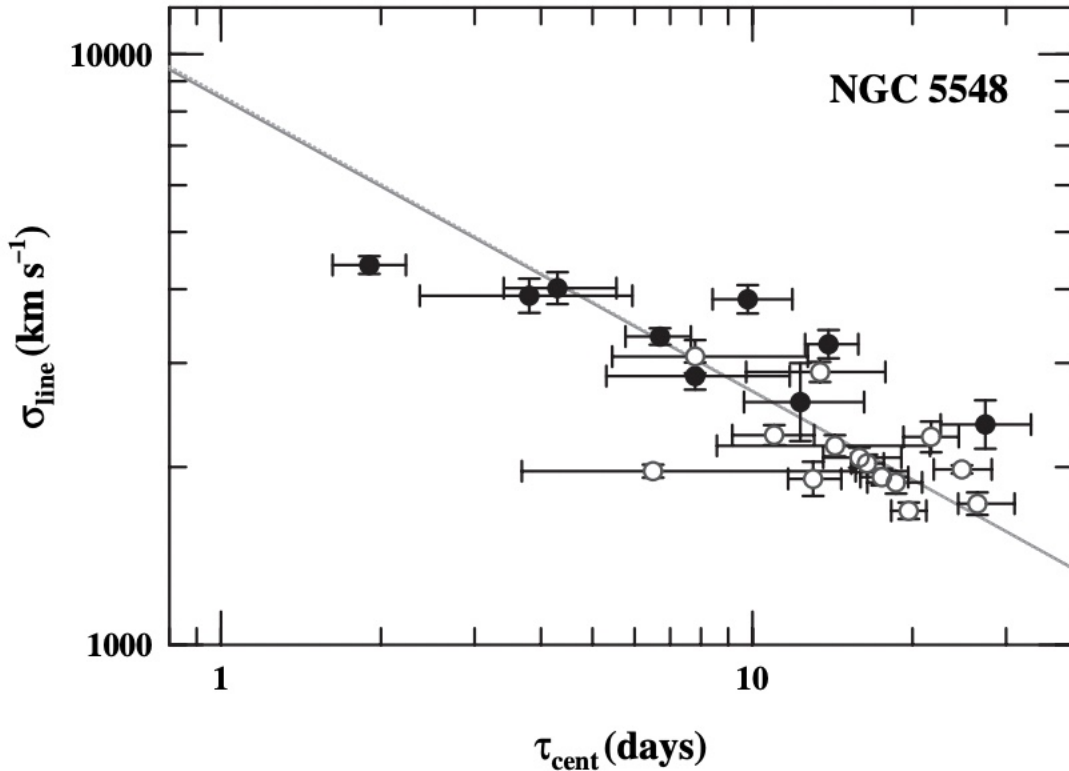


Figure 7

When emission-line time delays or lags were measured for multiple AGNs, the highest ionization emission lines were found to respond most rapidly to continuum variations, demonstrating clearly that there is ionization stratification within the BLR.

Moreover, the highest ionization lines tend to be broader than the lower ionization lines, and indeed a plot of line width versus time delay shows that the lag  $\tau$  varies with line width  $\Delta V$  as  $\tau \propto \Delta V^2$ , the virial relationship expected if the dynamics of the BLR is dominated by the gravitational potential of the central source.

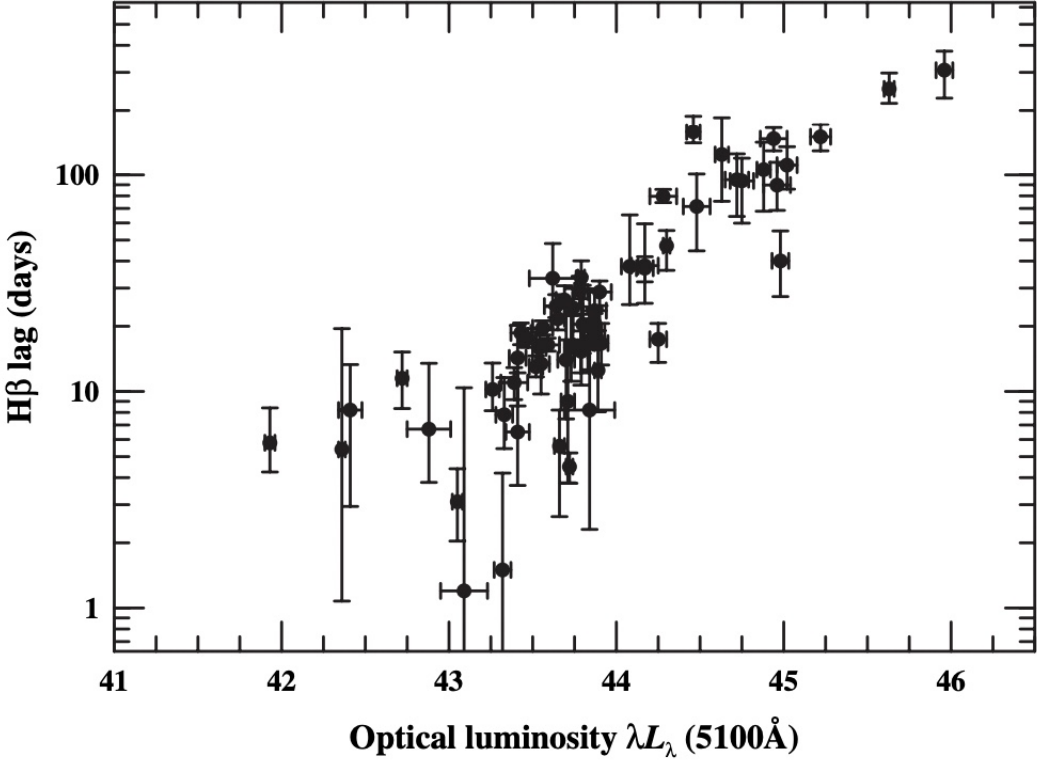


Figure 8

We might thus infer that, to some low order of approximation, their BLRs have similar physical conditions. We can thus easily reach the conclusion that there should be a very simple relationship between the size of the BLR and the AGN continuum luminosity as follows -

$$r \propto L^{1/2}$$

In figure 8, the observed slope of the correlation was found to be as  $r \propto L^{0.6 \pm 0.1}$ . This is surprisingly consistent with the very naive prediction of over four orders of magnitude in luminosity and time delays ranging from a few days to hundreds of days.

For AGNs with multiple reverberation measurements, there is virial relationship between line width and lag. This is strong evidence that the broad lines can be used to measure the mass of the central black hole via the virial theorem,

$$M_{bh} = \frac{f c \tau \Delta V^2}{G}$$

where  $f$  is a factor of order unity that depends on the unknown geometry and kinematics of the BLR. That these virial masses are valid at some level is demonstrated by the fact that a plot of the reverberation-based masses versus the stellar bulge velocity dispersion  $\sigma^*$  is consistent with the same  $M_{BH} - \sigma^*$  relationship seen in quiescent galaxies based on masses measured primarily by stellar or gas dynamics. Indeed, a mean value for the scaling factor  $f$  can be obtained by scaling the AGN  $M_{BH} - \sigma^*$  relationship to that for quiescent galaxies.

## 2 Extracting Data and Modelling

We used data from SDSS Dr16 dataset of quasars -

RMID	SDSS Identifier	RA	Dec	z
101	J141214.20+532546.7	213.0592	53.4296	0.458
191	J141645.58+534446.8	214.1899	53.7463	0.442
229	J141018.04+532937.5	212.5752	53.4937	0.47
267	J141112.72+534507.1	212.8030	53.7520	0.587
272	J141625.71+535438.5	214.1071	53.9107	0.263
694	J141706.68+514340.1	214.2778	51.7278	0.532
772	J142135.90+523138.9	215.3996	52.5275	0.249
840	J141645.15+542540.8	214.1881	54.4280	0.244

The spectra for each Quasar was first fitted for emission lines and continuum using PyQSOFit. It is a python software used to decompose the quasar spectrum. A step-by-step manual for the software states as follows :

- Principal Component Analysis(PCA) method is used for decomposing of the host galaxy and quasar component.
- The software fits the continuum for several components - Power Law, Polynomial, Fe II, Balmer Continuum.
- We fit line complexes one by one, including H, H, Mg II, C III], CIV and Ly complex. In each complex, broad and narrow Gaussian profiles are used to fit different emission lines.

### 2.0.1 PCA Method

Principal component analysis (PCA) is the process of computing the principal components and using them to perform a change of basis on the data, sometimes using only the first few principal components and ignoring the rest.

It is a dimensionality-reduction method that is often used to reduce the dimensionality of large data sets, by transforming a large set of variables into a smaller one that still contains most of the information in the large set. Because smaller data sets are easier to explore and visualize and make analyzing data much easier and faster for machine learning algorithms without extraneous variables to process.

## Step-by-step procedure of PCA

- Standardization
- Covariance Matrix Computation
- Computing the Eigenvectors and Eigenvalues of the covariance matrix to determine the principal components

Now, if we look over each step in detail, we have :

### 2.0.2 Standardization

The aim of this step is to standardize the range of the continuous initial variables so that each one of them contributes equally to the analysis.

If there are large differences between the ranges of initial variables, those variables with larger ranges will dominate over those with small ranges, which will lead to biased results. So, transforming the data to comparable scales can prevent this problem.

Mathematically, this can be done by subtracting the mean and dividing by the standard deviation for each value of each variable.

$$z = \frac{\text{value} - \text{mean}}{\text{standard deviation}}$$

### 2.0.3 Covariance Matrix

The aim of this step is to understand how the variables of the input data set are varying from the mean with respect to each other. Sometimes, variables are highly correlated in such a way that they contain redundant information. So, in order to identify these correlations, we compute the covariance matrix.

$$\begin{bmatrix} \text{cov}(x, x) & \text{cov}(x, y) & \text{cov}(x, z) \\ \text{cov}(y, x) & \text{cov}(y, y) & \text{cov}(y, z) \\ \text{cov}(z, x) & \text{cov}(z, y) & \text{cov}(z, z) \end{bmatrix}$$

The covariance matrix is a  $p \times p$  symmetric matrix, where  $p$  is the number of dimensions. We note that here :  $\text{cov}(a,a) = \text{var}(a)$  and  $\text{cov}(a,b) = \text{cov}(b,a)$ .

### 2.0.4 Computing Eigenvectors and Eigenvalues

Principal components are new variables that are constructed as linear combinations or mixtures of the initial variables. These combinations are done in such a way that the new

variables (i.e., principal components) are uncorrelated and most of the information within the initial variables is squeezed or compressed into the first components.

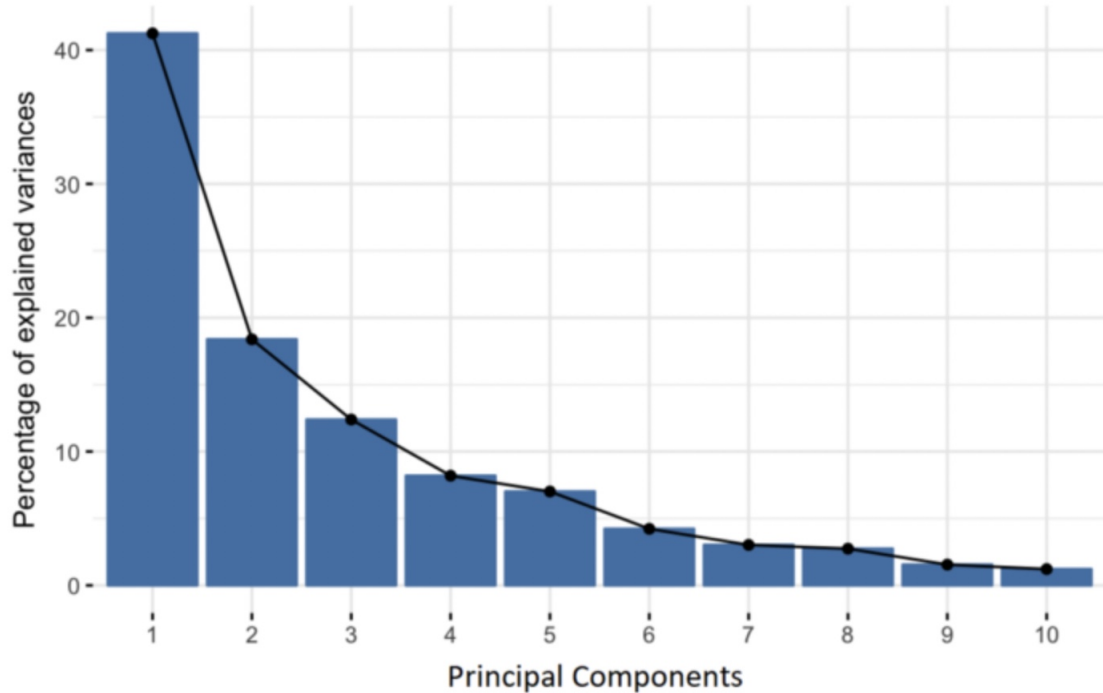


Figure 9: Percentage of Variance (Information) for each by PC

Organizing information in principal components this way, will allow you to reduce dimensionality without losing much information, and this by discarding the components with low information and considering the remaining components as your new variables.

Geometrically speaking, principal components represent the directions of the data that explain a maximal amount of variance, that is to say, the lines that capture most information of the data. The relationship between variance and information here, is that, the larger the variance carried by a line, the larger the dispersion of the data points along it, and the larger the dispersion along a line, the more the information it has.

- As stated before, the python package PyQSOFit was used to perform the spectral analysis for different RMIDs - here, we have the observation for an epoch ranging for about 70 days for each quasar. When one performs the spectral analysis over one of the spectrum obtained, we have something like this -

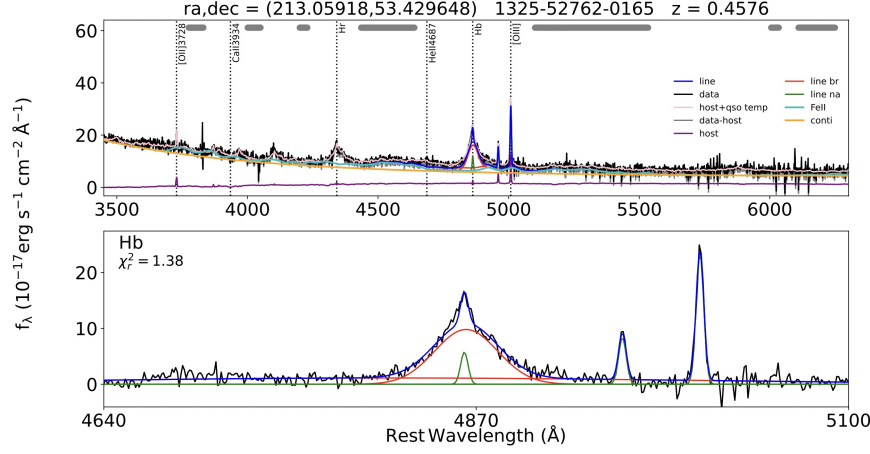


Figure 10: Example of Spectral analysis of one of the observations of RMID-101

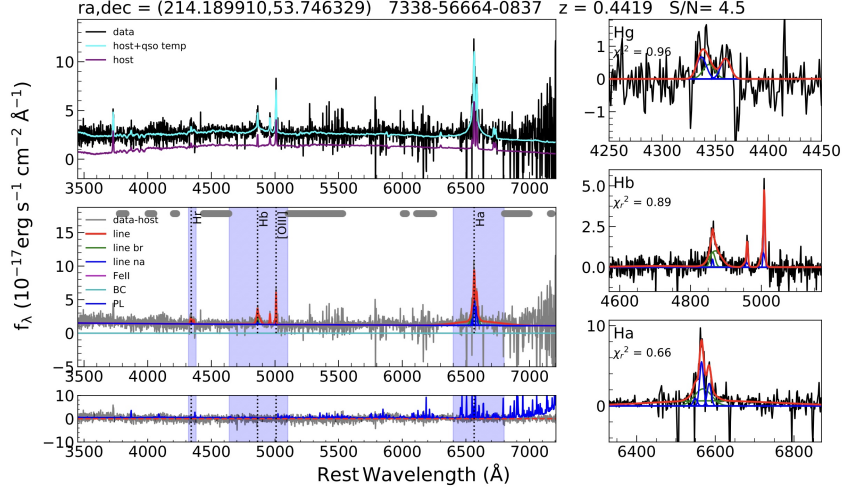


Figure 11: Example of Spectral analysis of one of the observations of RMID-191

The code hence performs these steps (in simple terms) - first, it loads the line list file, containing lines and their constraints, which will be needed in the fitting program. Second, it reads the spectrum fits file. Third, it finally fits the different components by using lam, flux, err, z, and other optional parameters that we input.

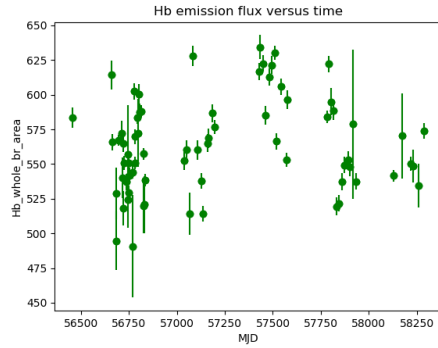
**NOTE :** It fits the different narrow line and broad line emissions with different gaussians - a double gaussian or a single, etc.

### 3 Data Analysis and Results

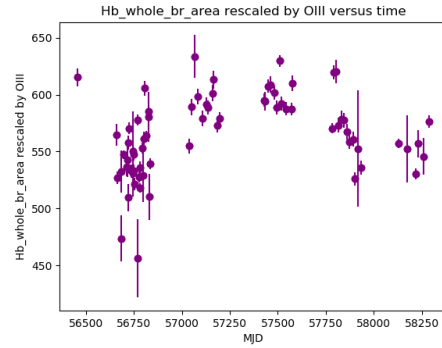
From the spectral fitting, we can calculate the emission flux related to different emission lines. Now, plotting the flux versus time for a particular emission line of a particular quasar gives us the trend in the properties.

### 3.0.1 RMID-101 Results

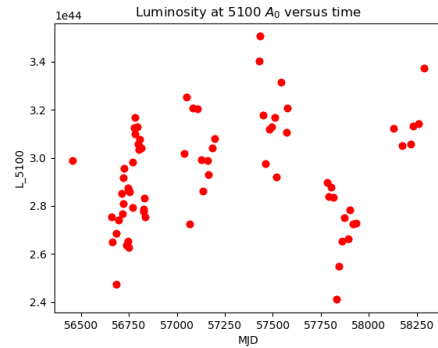
For RMID - 101, we have :



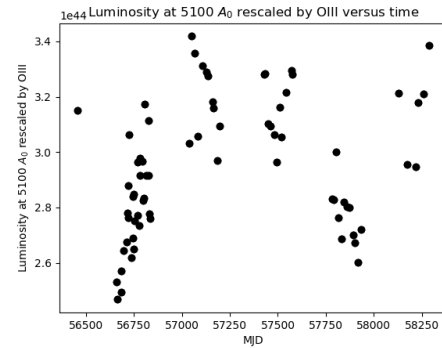
(a) Hbeta flux versus time



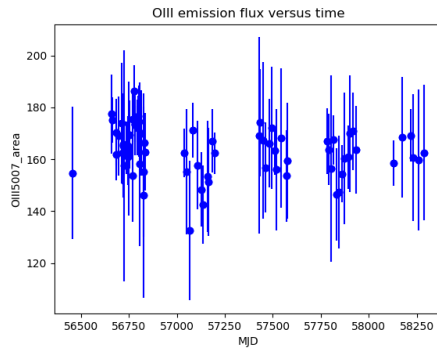
(b) Hbeta flux rescaled wrt OIII versus time



(c) L5100 versus time

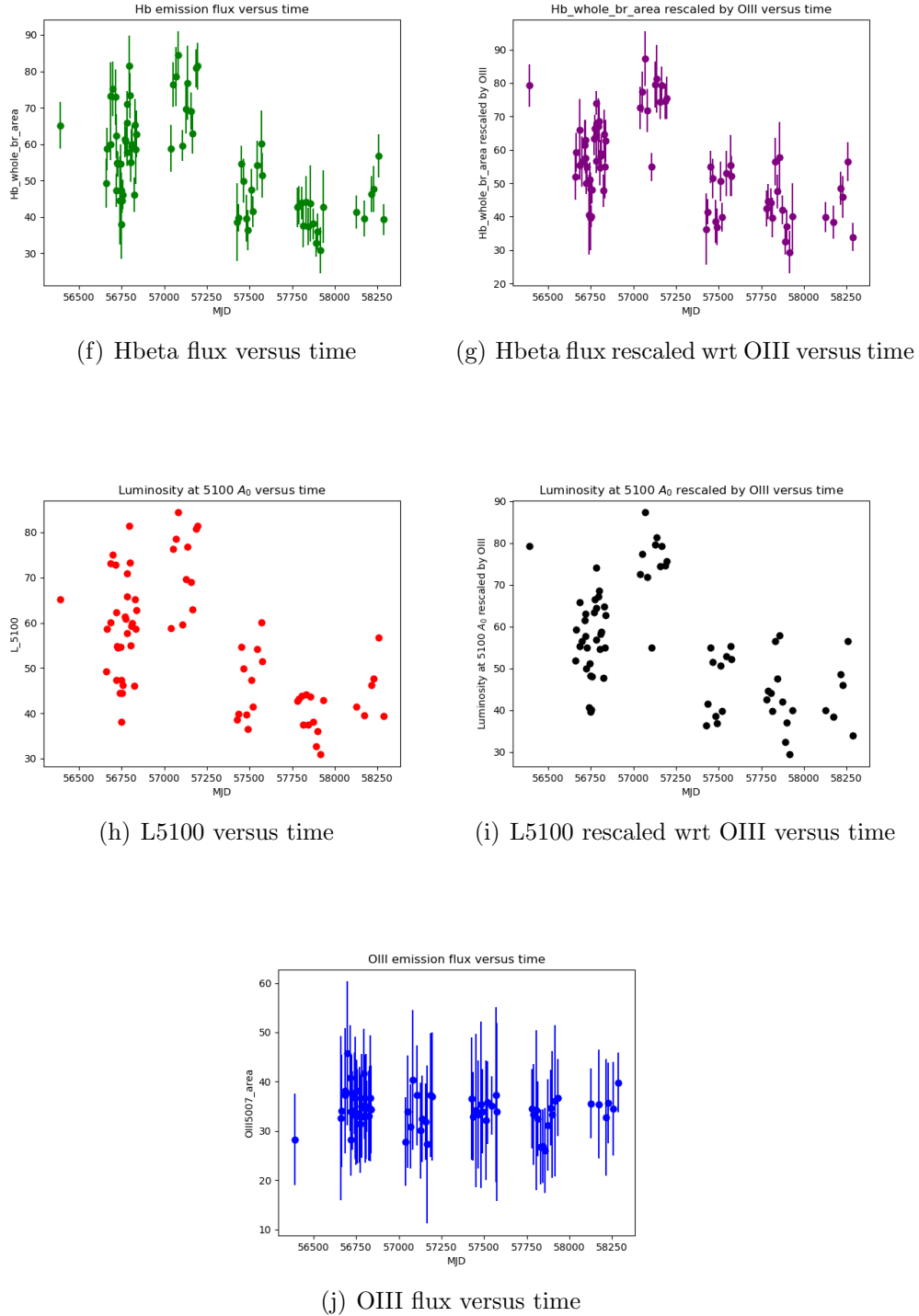


(d) L5100 rescaled wrt OIII versus time

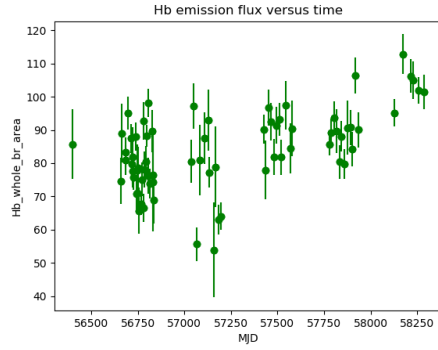


(e) OIII flux versus time

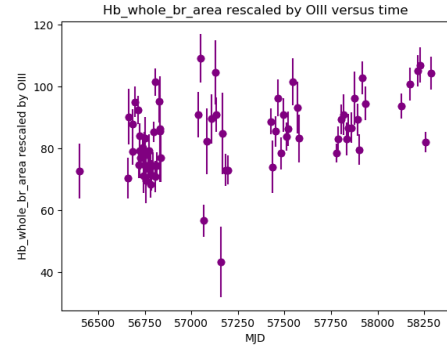
### 3.0.2 RMID-191 Results



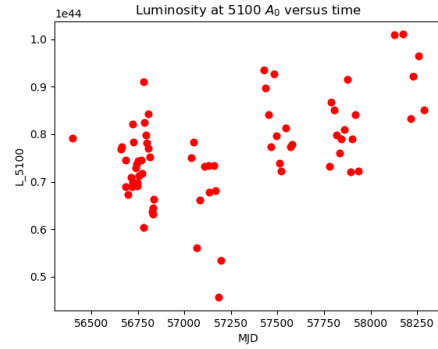
### 3.0.3 RMID-229 Results



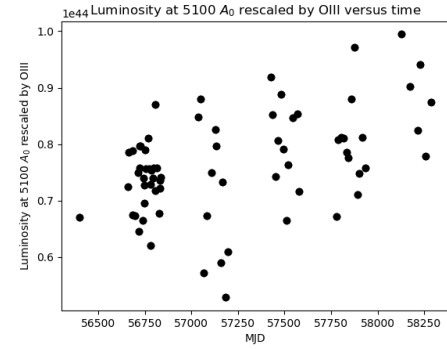
(k) Hbeta flux versus time



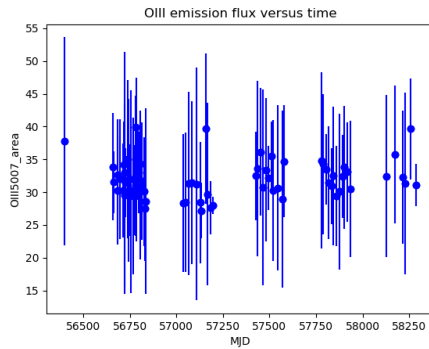
(l) Hbeta flux rescaled wrt OIII versus time



(m) L5100 versus time

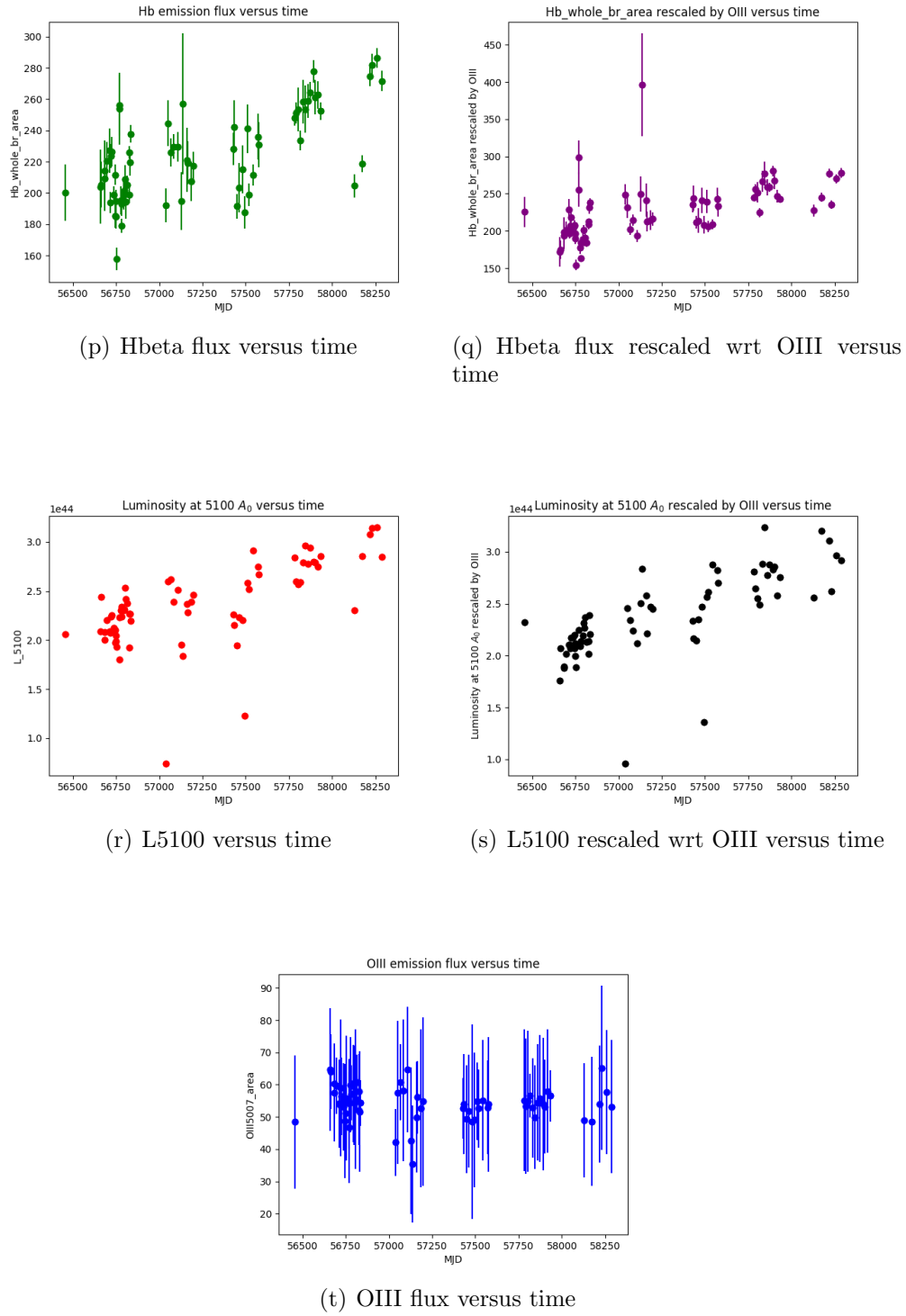


(n) L5100 rescaled wrt OIII versus time

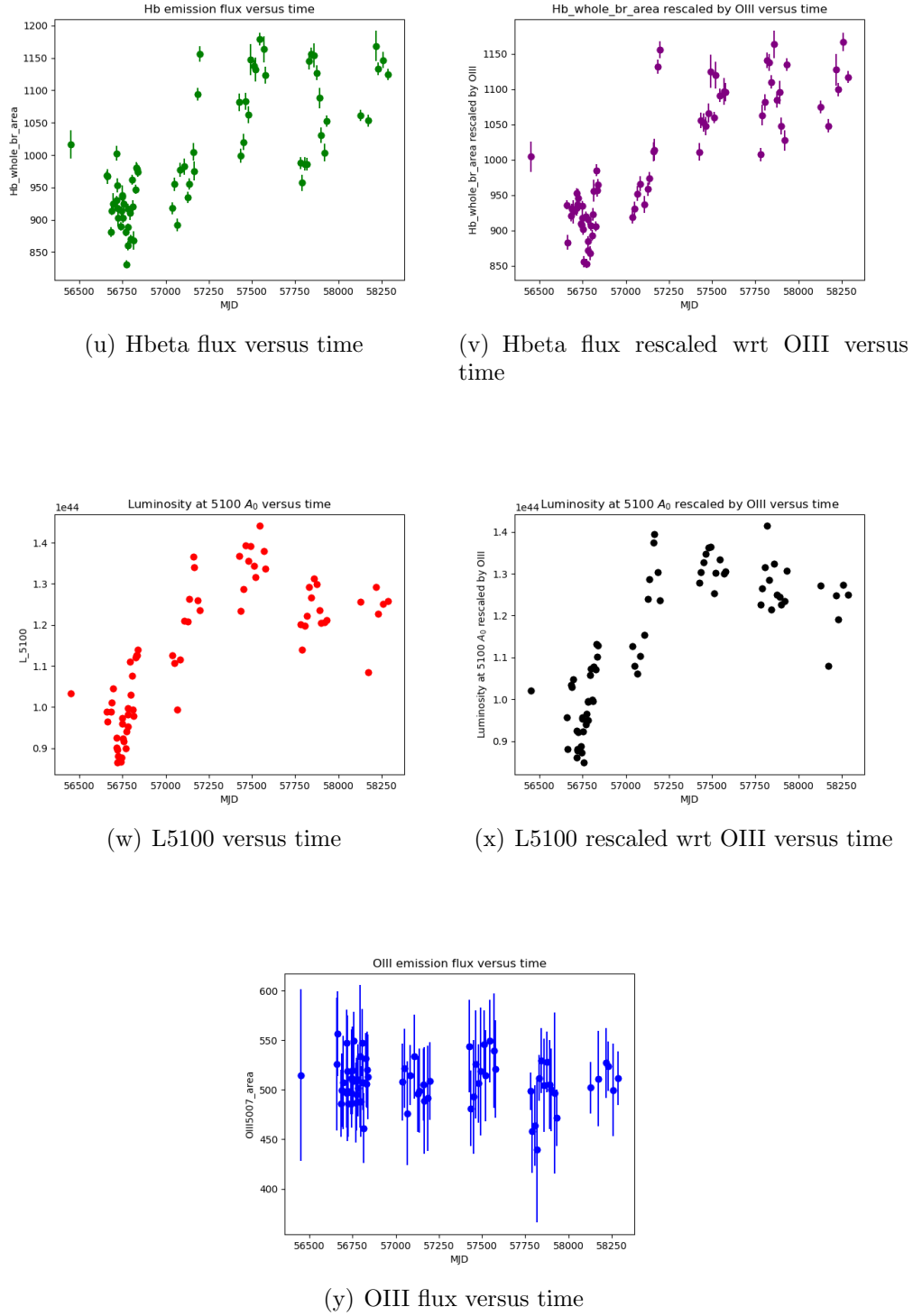


(o) OIII flux versus time

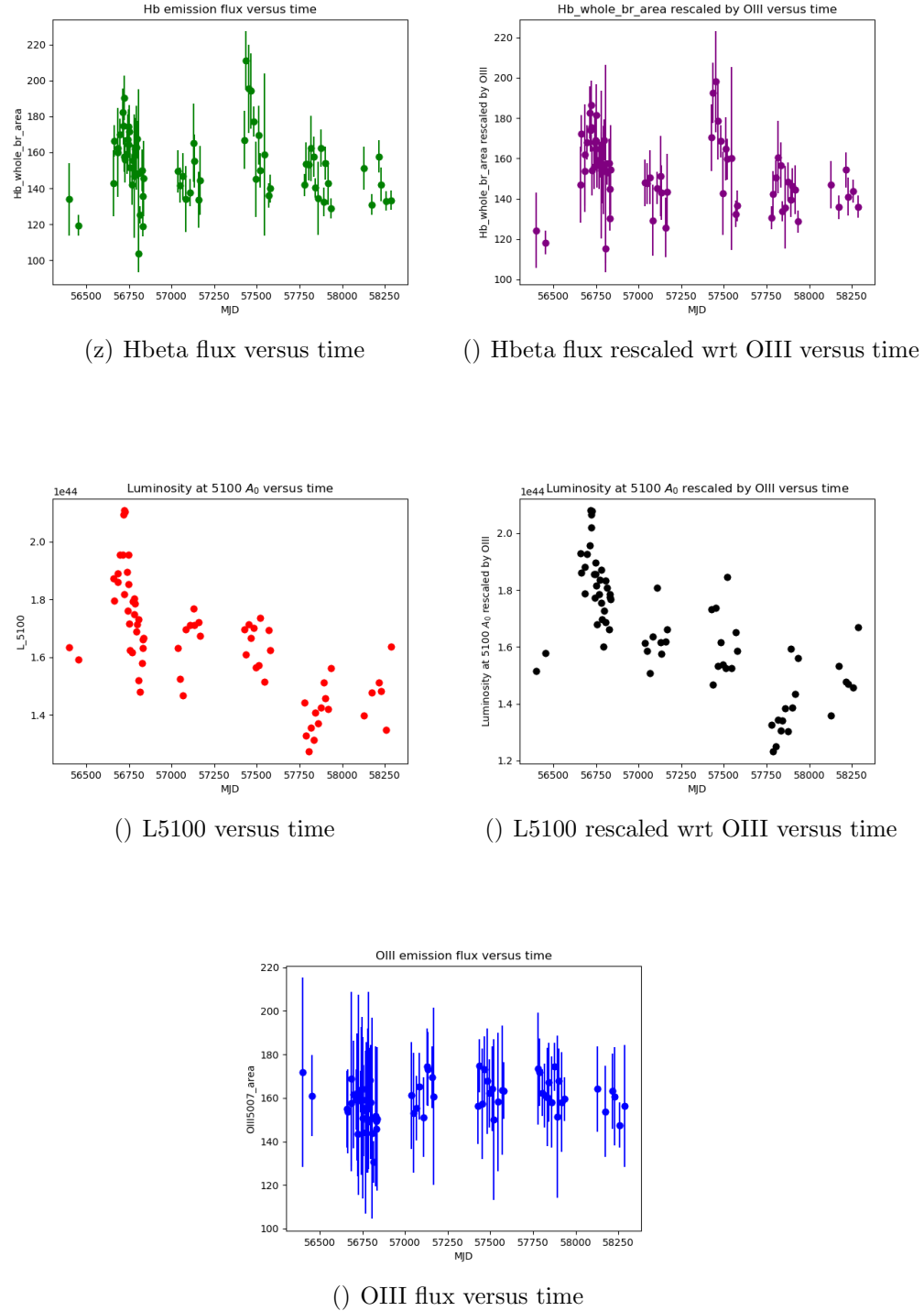
### 3.0.4 RMID-267 Results



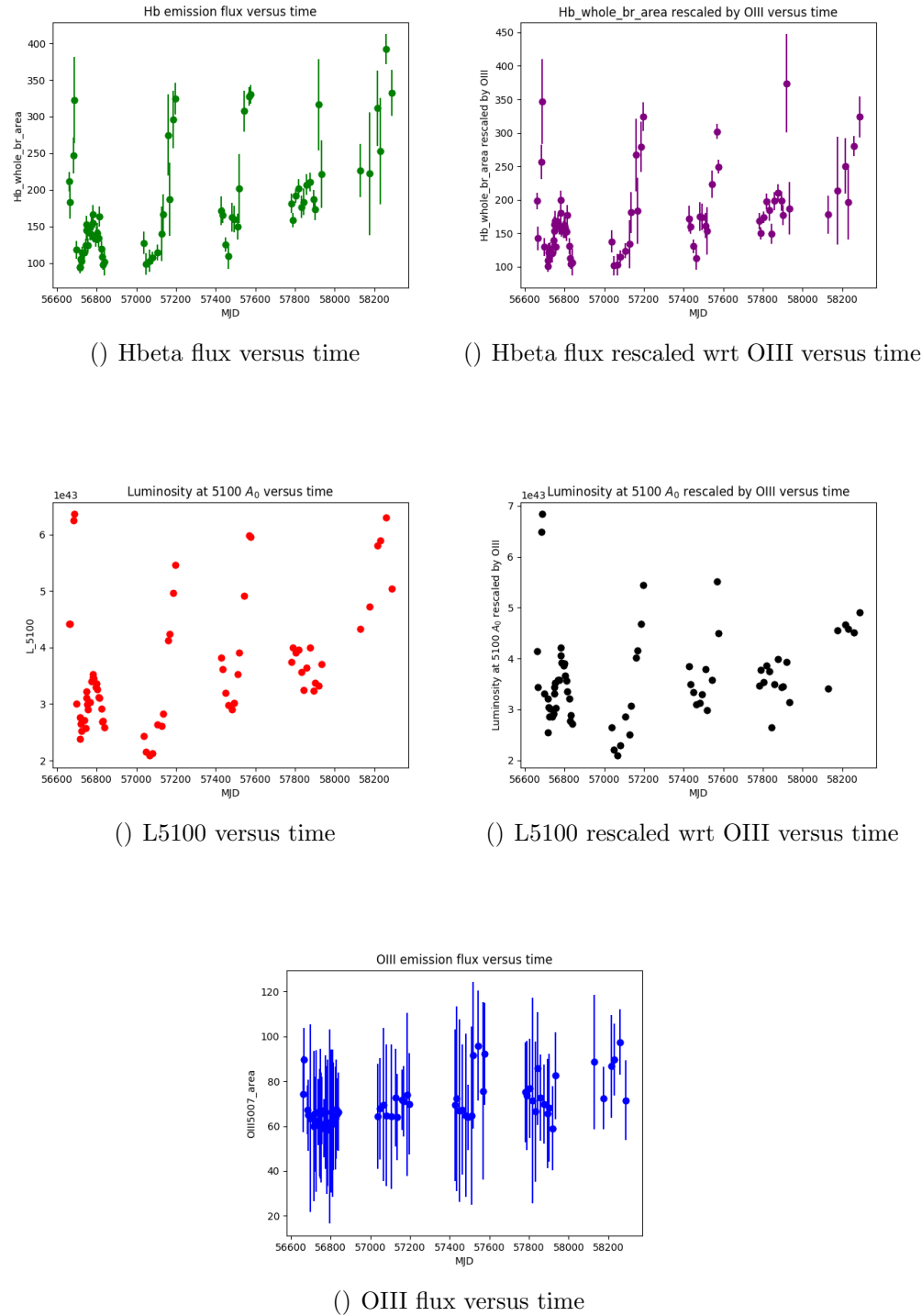
### 3.0.5 RMID-272 Results



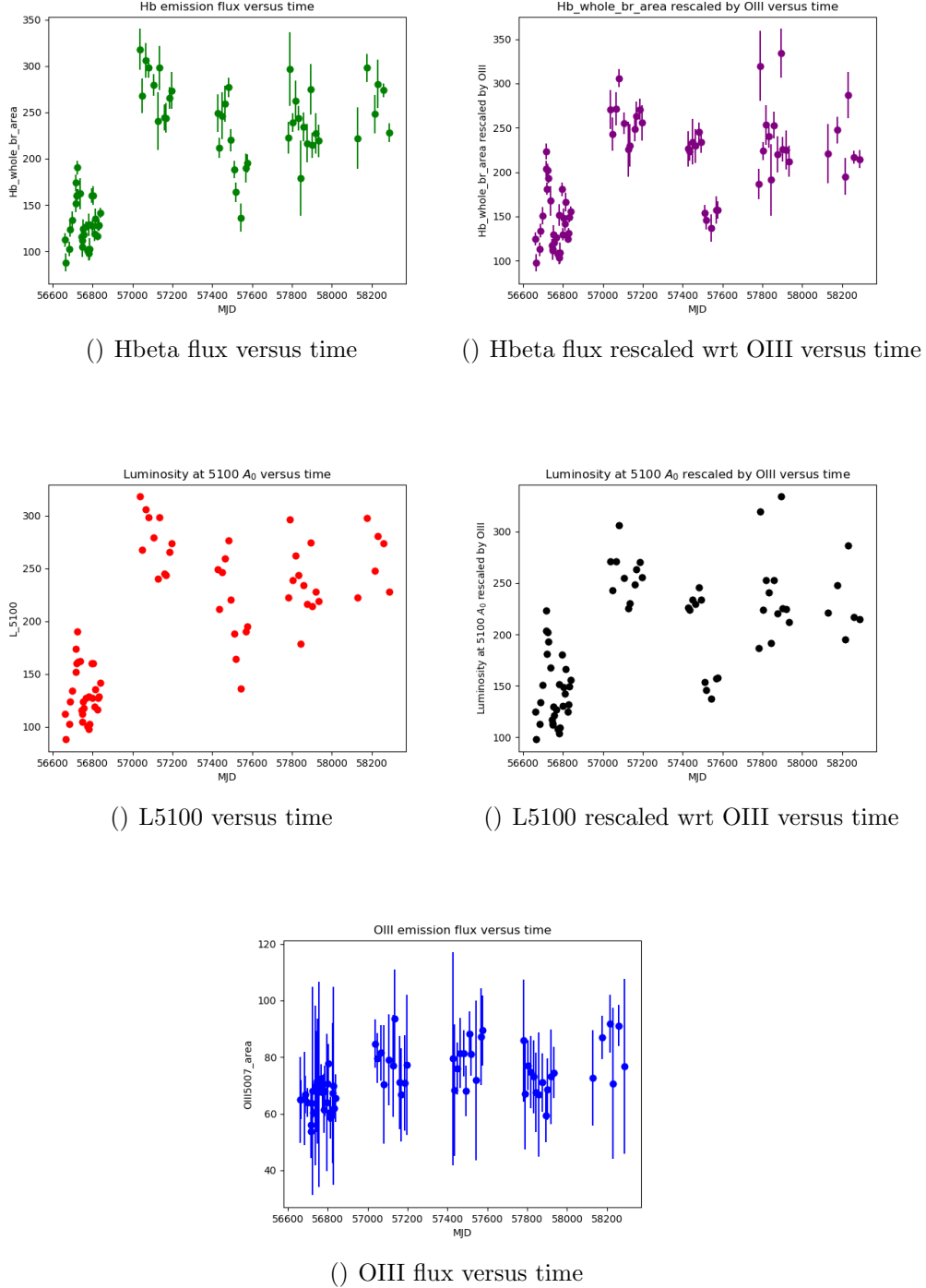
### 3.0.6 RMID-694 Results



### 3.0.7 RMID-772 Results



### 3.0.8 RMID-840 Results



## 4 Lag Measurements

Further analysing the properties of spectrum requires us to measure the lag or simply, the time delays between different bands. The main aim of spectroscopic monitoring campaigns

has been to determine the response of the broad emission lines to continuum variations and thus determine the structure and kinematics of the line-emitting gas through the process of “reverberation mapping”. Now, the most common way of calculating this time lag is by the cross-correlation function. In terms of statistics, cross correlation provides a means to find the association between signals. Cross-correlation is basically the method by which we see how similar a set of numbers are and how this can be quantified. This requires two curves such that their peaks can be assessed.

This technique is based on the fact that if one carries out a point by point multiplication of two data sets, the sum of these products would be the quantification of the relationship between two sets.

$$r_{xy} = \sum_{i=0}^{N-1} x_i y_i \quad (1)$$

where  $N$  is the number of data points,  $x_i$  is the  $i$ th point of the first data series and  $y_i$  is the  $i$ th point of the second data series. And  $r_{xx}$  is the correlation.

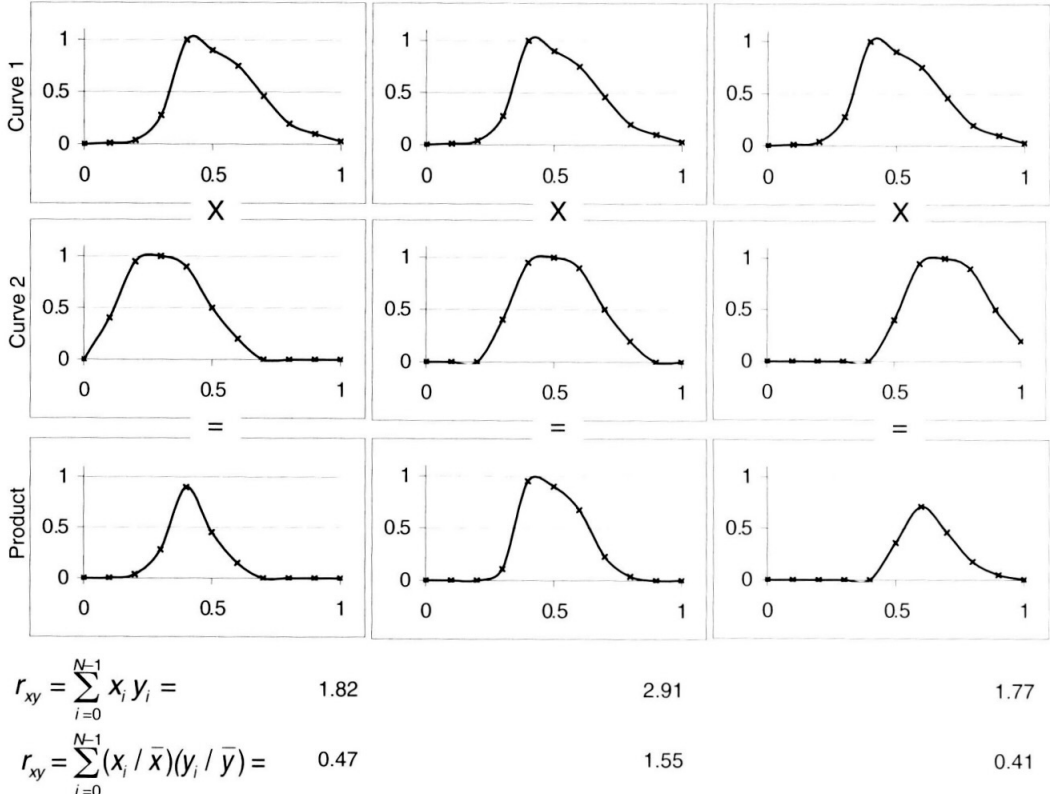


Figure 12: The effects of time series shifts on the cross-correlation.

It is common practice to time-shift one curve II of figure 12. The number of data points by

which the curve is shifted by is called the LAG, denoted by  $\ell$ .

$$r_{xy}(\ell) = \sum_{i=0}^{N-1} x_i y_{i+\ell} \quad (2)$$

The issue with equation 2 is that its not unit less. Hence, most people normalize it by dividing by the square root of the product of autocorrelation of x at zero lag and autocorrelation of y at zero lag.

$$\rho_{xy}(\ell) = \frac{r_{xy}(\ell)}{\sqrt{r_{xx}(0)} \sqrt{r_{yy}(0)}} \quad (3)$$

**NOTE :** Auto-correlation of a data set is simply the cross relation done with itself.

## 4.1 Errors in Lag Measurements

There is no specific way to calculate the uncertainties in cross correlation lags, but the most famous one is monte carlo simulations. The steps in MC Simulations are :

- Adopting a model light curve that is supposed to drive the other variations.
- The driving light curve is then convolved with a transfer function that produces a responding light curve, which most often represents the response of a broad emission line to the continuum variations.
- The driving and responding light curves are then “sampled” in a fashion that somehow mimics the real observations, and then the effects of observational uncertainties, both random and systematic, are included.
- These artificial data sets are then cross-correlated as if they were real data, and the cross-correlation lag is recorded.
- This process is repeated a large number of times to build up a cross-correlation peak distribution (CCPD).

## 4.2 Lag Measurement for our data

Now, we calculated the lag between the L5100 curve and the H beta continuum curve using the ccf code written in python. The source can be found here - <http://ascl.net/code/v/1868>. For more details on the theory - one can look over the paper cited at [4].

### Notes for The Readers

For the readers who would like to follow up on this work, there are certain things one should note :

- The lag can only be calculated when the number of data points is sorted in ascending order or an increasing order according to the MJD(time).

- One needs to be careful while choosing the lag range i.e. - the time period to get an appropriate correlation measure between the two datasets.

Now, we'll try to look over the lag measurements of some of the RMIDs that were used. One can use the Github repository to calculate the lag between the other ids.

#### 4.2.1 RMID - 101

For RMID-101, the lag for all data points was found as follows :

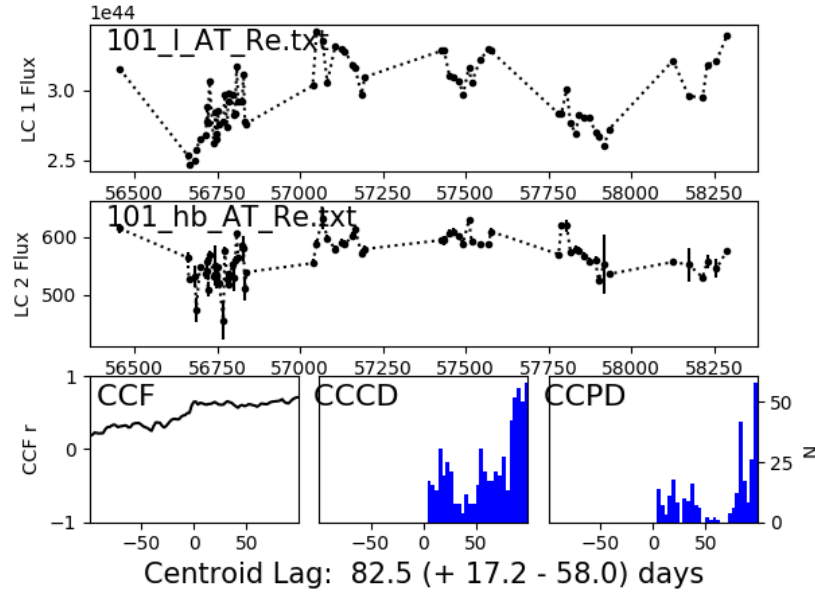


Figure 13: Lag measurement for 71 MJDs - that is all the data points

In order to compare our lag measurement with the one in the paper [2], we take only 30 points near 56750 MJD.

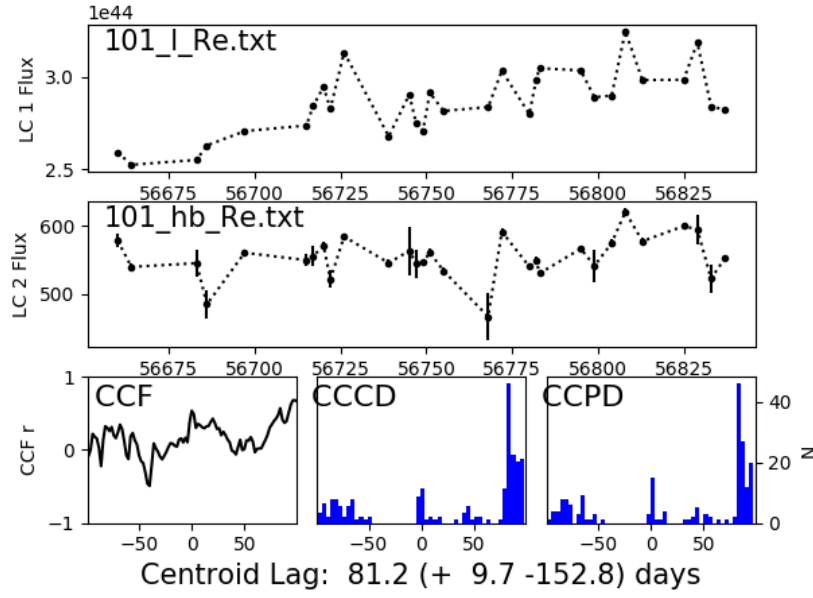


Figure 14: Lag measurement for 30 MJDs - near 56750

#### 4.2.2 RMID - 191

The lag for full data points i.e. - 70 points is as follows :

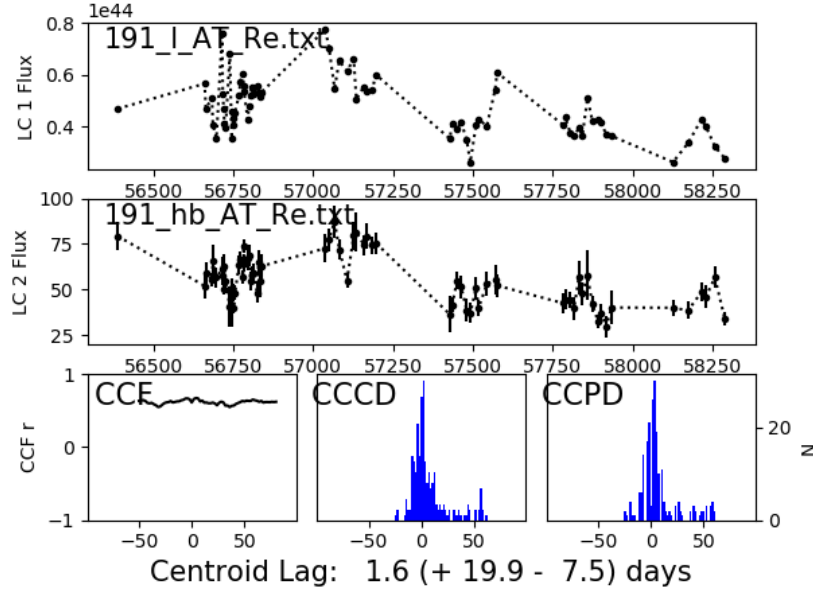


Figure 15

#### 4.2.3 RMID-229

The lag for full data points i.e. - 70 points is as follows :

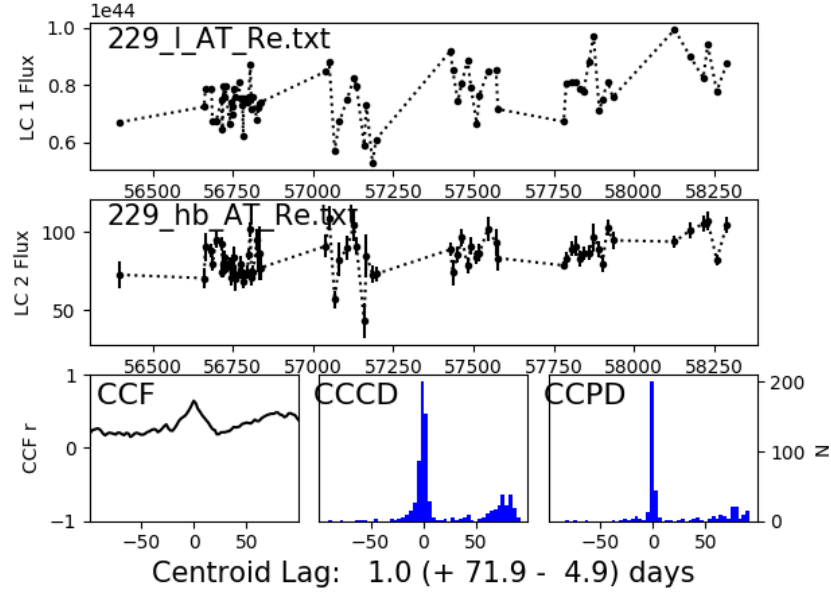


Figure 16

In order to compare our lag measurement with the one in the paper [2], we take only 30 points near 56750 MJD.

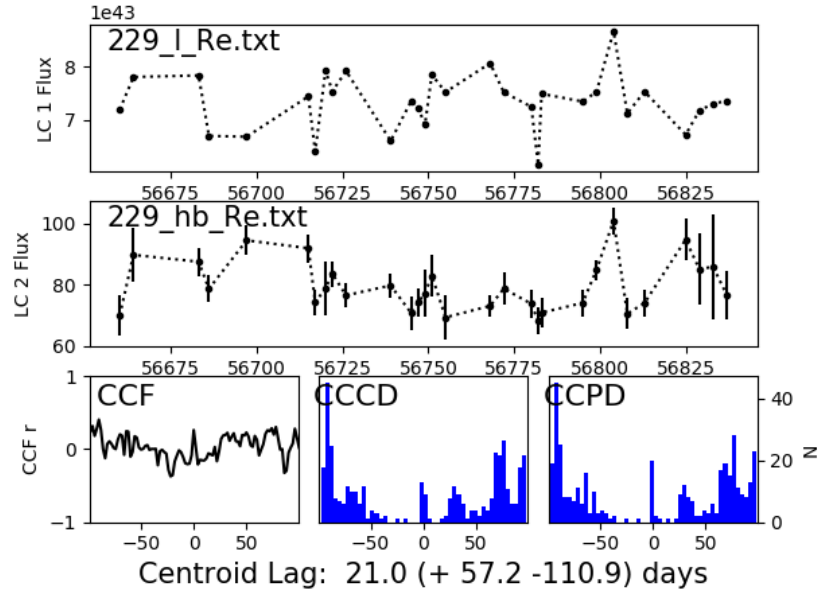


Figure 17

#### 4.2.4 RMID-267

The lag for full data points i.e. - 70 points is as follows :

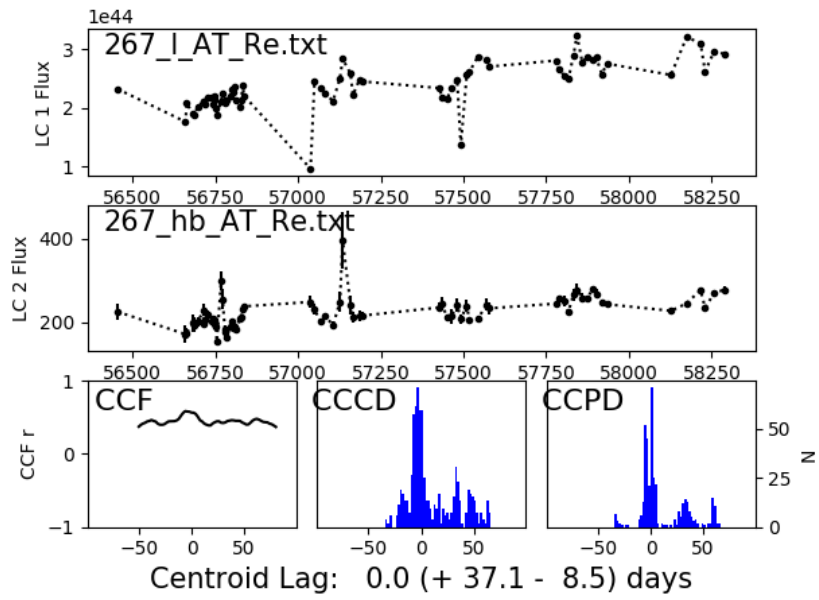


Figure 18

## 5 Discussion

By far, this might be the most important section in this report. We would begin by looking over some of the data analysis of the RMIDs and compare it with the paper - [2].

Let's look over the RMID 101 which is considered as the best sample by [2]. We first note the following -

- The data we are using contains about 70 to 72 points collected from the emission fluxes from 70 to 72 observations.
- The data used in the paper [2] has used around 30 to 32 points which has the range of - 56500 and 57000.

Hence, in order to compare the analysis we take the data points in this area and try to see the difference between the two analysis -

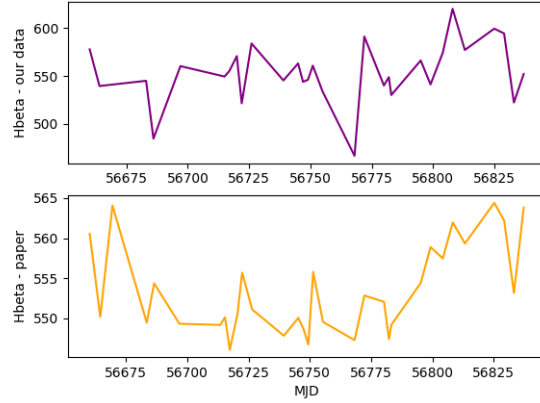


Figure 19

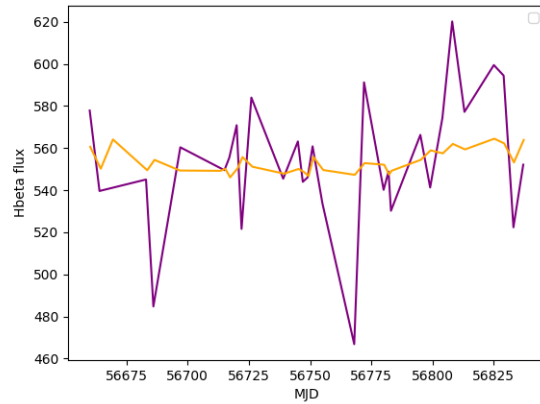


Figure 20

19 shows us the Hbeta emission flux of the RMID-101 obtained from our data analysis and as given in the paper. 20 shows us the overplot between the same. We are not very sure as to why the analysis is giving us different results. There is also something important to be noted here - the paper at the time of it's publication had access to a largert observation set but chose to use only 30 days of observations. We aren't very sure about it either.

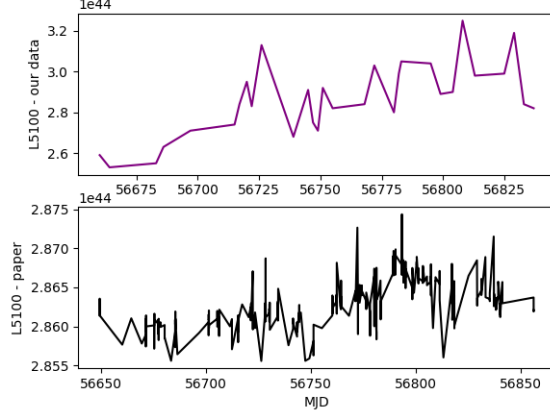


Figure 21

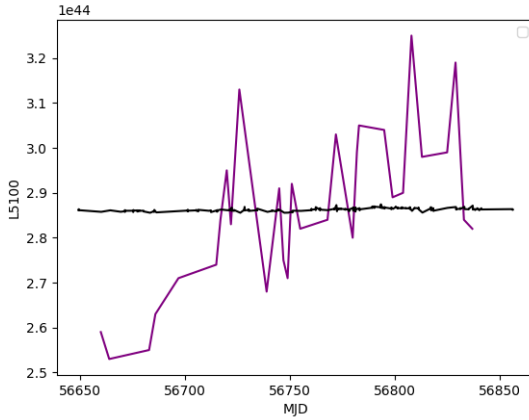


Figure 22

21 shows us the trend for L5100 for our data and the paper data as obtained from the g-bands as provided on the source. 22 shows us the overplot of the same. It's important to note for the readers who would like to further add to this work that the data from the paper was taken from all the telescopes(in order to avoid any confusion).

Finally we look over the trend between the Hbeta line flux and L5100 for RMID-101 for our data -

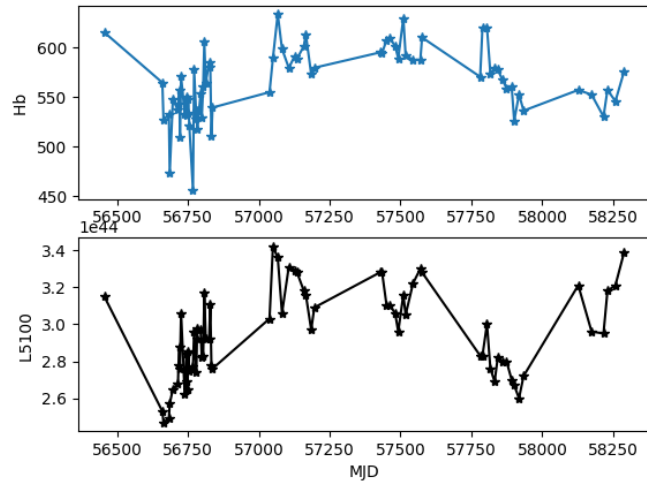
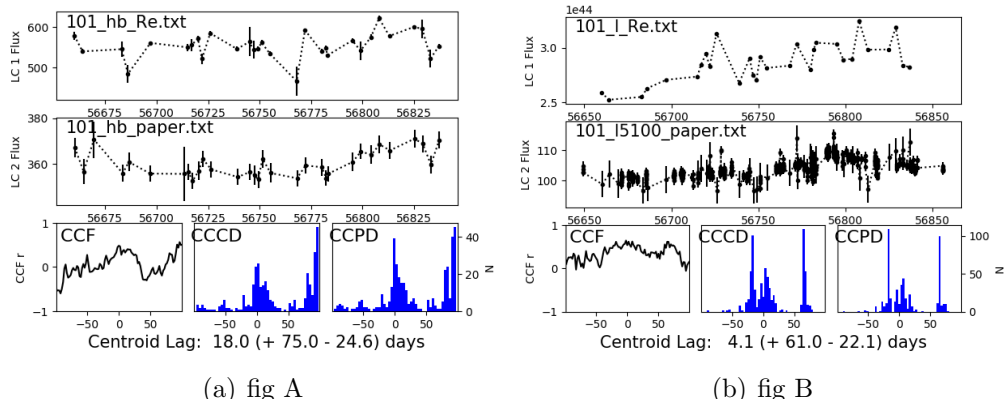


Figure 23

We could not find any visible lag between the two plots and hence, we were getting bad cross-correlation functions for them.

Looking over the issues in lag measurements and how it was explored in this study, we again take the example of 101 as it being the best sample according to [2].



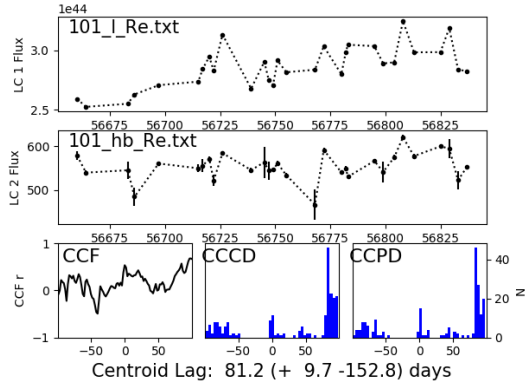


Figure 24

In order to compare our analysis with the paper - we further tried to calculate the Lag between the H $\beta$  emission lines from our analysis and the paper in ?? and same for L5100 in ???. We see around 18 and 4.3 days, respectively; which shows that the analysis definitely is giving us some different results.

24 shows us the Lag calculation using CCF code but for the range - used in the paper for our data- however, that did not give us a very different number from that in figure 13.

## 6 Acknowledgements

I am extremely grateful for this opportunity to be working on this project with Dr. Suvendu Rakshit, Aryabhatta Research Institute of Observational Sciences, Nainital. This project explored various techniques involved Reverberation mapping of AGNs, instilled wonderful insights about the astrophysics of Broad line region.

I am thankful to my supervisor, who provided me with proper guidance and direction, by making time, despite their busy schedule. I would also like to thank Ms. Shivangi Pandey, a PhD student at ARIES, at helping me understand various aspects of codes and softwares and advising me regarding it.

This project used data from Sloan Digital Sky Survey(SDSS)is a major multi-spectral imaging and spectroscopic redshift survey using aN optical telescope at New Mexico, United States. We also had significant help from the PyQSOFit to calculate the various properties of spectrum, explained in the paper - .

Thankfully,  
Aditi Sinha

## References

- [1] K. D. Denney et al. “Reverberation Mapping Measurements of Black Hole Masses in Six Local Seyfert Galaxies”. In: 721.1 (Sept. 2010), pp. 715–737. DOI: 10.1088/0004-637X/721/1/715. arXiv: 1006.4160 [astro-ph.CO].
- [2] C. J. Grier et al. “The Sloan Digital Sky Survey Reverberation Mapping Project: H $\alpha$  and H $\beta$  Reverberation Measurements from First-year Spectroscopy and Photometry”. In: 851.1, 21 (Dec. 2017), p. 21. DOI: 10.3847/1538-4357/aa98dc. arXiv: 1711.03114 [astro-ph.GA].
- [3] Hengxiao Guo, Yue Shen, and Shu Wang. *PyQSOFit: Python code to fit the spectrum of quasars*. Astrophysics Source Code Library, record ascl:1809.008. Sept. 2018. ascl: 1809.008.
- [4] Bradley M. Peterson et al. “On Uncertainties in Cross-Correlation Lags and the Reality of Wavelength-dependent Continuum Lags in Active Galactic Nuclei”. In: *Publications of the Astronomical Society of the Pacific* 110.748 (June 1998), pp. 660–670. DOI: 10.1086/316177. URL: <https://doi.org/10.1086%2F316177>.
- [5] Suvendu Rakshit, C. S. Stalin, and Jari Kotilainen. “Spectral Properties of Quasars from Sloan Digital Sky Survey Data Release 14: The Catalog”. In: 249.1, 17 (July 2020), p. 17. DOI: 10.3847/1538-4365/ab99c5. arXiv: 1910.10395 [astro-ph.GA].
- [6] Suvendu Rakshit et al. “The Seoul National University AGN Monitoring Project. II. BLR Size and Black Hole Mass of Two AGNs”. In: 886.2, 93 (Dec. 2019), p. 93. DOI: 10.3847/1538-4357/ab49fd. arXiv: 1910.02412 [astro-ph.GA].